Rapid Communications

Unveiling the mechanism of wave-front distortion of superfluorescent pulses

Kenta Kitano* and Haruka Maeda
Department of Physics and Mathematics, Aoyama Gakuin University, Kanagawa 252-5258, Japan

(Received 8 April 2019; published 31 October 2019)

We investigated the transverse properties of 420-nm yoked superfluorescence (YSF) emitted from the atomic vapor of rubidium by driving the 5*S*-5*D* two-photon transition with an ultrashort laser pulse. From the observed interferograms of the superfluorescent pulses, we derived both the amplitude and phase properties of their electric fields. By increasing the pump-pulse intensity, the spatial profile of the 420-nm YSF changed from a central bright spot into a ring-shaped radial profile, accompanied by a simultaneous distortion of the wave front. This behavior can be explained by considering the intensity-dependent phase shifts of the 5*S*-5*D* wave packets during the excitation process, which was further imprinted to the 420-nm YSF wave front. The single-shot experiments enabled us to clarify the locally coherent regions of the 420-nm YSF as well as their stochastic feature.

DOI: 10.1103/PhysRevA.100.041803

Superfluorescence (SF) is cooperative spontaneous radiation emitted from an ensemble of two-level systems, which is initially prepared in its excited state without any coherence [1]. The underlying physics of SF is the photon-mediated interaction between atoms in the many-body system, which has been investigated not only in traditional gaseous atomic and molecular systems but also in a variety of cutting-edge experiments concerning trapped ions [2,3], circuit QED [4], nitrogen-vacancy centers in diamond [5,6], single-atom injections to the optical cavity [7], and trapped cold atoms in the optical bad cavity [8].

In the case of a large sample produced by a laser pulse, a SF medium is often prepared in a so-called pencil-shaped sample [see Figs. 1(a) and 1(b)]. For such a sample, the geometrical properties of SF can be classified according to the Fresnel number defined by $F = \pi\omega^2/\lambda L$, where $\pi\omega^2$, L, and λ are the sample area, the sample length, and the wavelength of the SF, respectively [9]. For $F \gg 1$, where the diffraction angle ($\theta_{\mathrm{d}} = \lambda/\pi\omega$) is smaller than the geometrical angle ($\theta_{\mathrm{G}} = \omega/L$), multiple off-axis modes are permitted [see Fig. 1(a)], resulting in multiple coherent areas in the transverse plane. Furthermore, since practical pump pulses have Gaussian intensity profiles in the transverse plane, the initial population-inversion densities as well as the SF dynamics are radially dependent. However, these transverse effects are in most cases smeared out because of the spatial averaging and the diffraction coupling in the SF process [9,10].

Yoked superfluorescence (YSF) originates in the interplay between spontaneously developed and initially prepared coherence [11]. Consider a case where a three-level system is initially prepared in a coherent superposition of the ground and the excited states [see the transition indicated by the red arrows in Fig. 1(c)]. If the SF emerges from the transition between the excited and the intermediate states ["upper SF," indicated by the orange arrow in Fig. 1(c)] within the decoherence time of the system, it simultaneously brings about coherence between the intermediate and the ground states, resulting in a coherent pulse emission in association with the transition between the two states ["lower SF," indicated by the blue arrow in Fig. 1(c)]. These paired emissions are called YSF, which can be conceptualized as a time-delayed four-wave mixing (FWM) process [12]. While the temporal characteristics of YSF have been extensively studied [13,14], few reports have focused on the geometrical properties of YSF, such as emission angles or beam profiles in the transverse plane. For the former properties, it was demonstrated that lower SF is highly directional to satisfy the phase-matching condition in FWM, whereas an upper SF is omnidirectional [12,15]. This suggests that, for lower SF, the off-axis modes are suppressed by the additional constraint of the beam divergence angle for FWM, θ_{FWM}, as illustrated in Fig. 1(b). For the latter properties, on the other hand, the lower SF emitted from the different concentric cylindrical shells was observed without significant obscuration [16]. Particularly, when the pulse area at the beam center was larger than π, the lower SF showed a pattern of concentric rings, as predicted in Ref. [17].

To realize SF as a well-defined coherent light source, we aim to understand the phase properties of the SF electric fields as well as their shot-to-shot fluctuation in relation to the geometric beam profile of the SF reported in Ref. [16]. More specifically, the fundamental questions that we hope to solve are twofold: The first question is whether the YSF fields are entirely or locally coherent in the transverse beam profile and the manner in which they change shot-to-shot, whereas the second question is whether the wave front in the coherent area is flat or distorted and the mechanism that is used to determine that. To find the answers to these questions, we apply in our experiments wave-front interferometry to the lower SF fields.

Figure 1(c) presents the atomic configuration and the radiation fields associated with the YSF of rubidium (Rb) atoms. The atoms were excited from the 5*S* ground state to the 5*D* excited state via a two-photon absorption with a femtosecond laser pulse, creating a superposition between the two states. The subsequent decay process accompanied

*kkitano@phys.aoyama.ac.jp

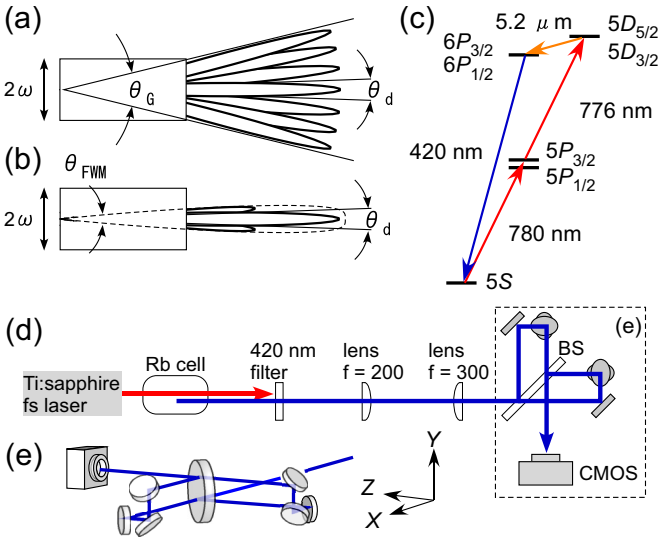

FIG. 1. Schematic representation of the SF field (a) and the lower SF field of the YSF (b) emitted from the pencil-shaped sample for a large Fresnel number configuration. (c) Energy diagram of Rb and the related transitions. (d) A schematic of the experimental setup. (e) Michelson interferometer.

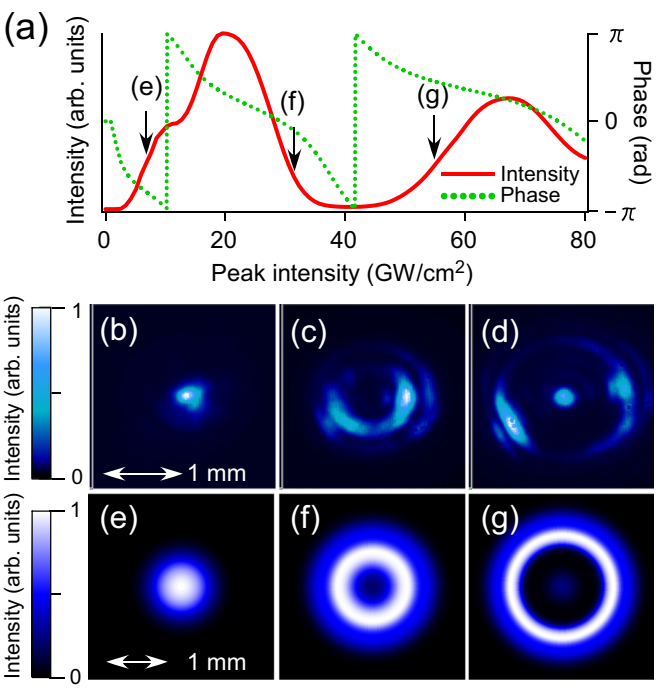

FIG. 2. (a) Calculated blue-light intensity and its phase plotted as a function of the pump-pulse peak intensity. Blue-light intensity profiles recorded at various pump-pulse powers of 19 mW (b), 88 mW (c), and 155 mW (d). (e)–(g) Blue-light intensity profiles simulated at the different pump-pulse intensities indicated in (a).

radiations with wavelengths of 5.2 μm (infrared light) on the 5D-6P transition and 420 nm (blue light) on the 6P-5S transition. In the present experiment, only the blue-light emission was observed. A schematic of the experimental setup is depicted in Fig. 1(d). We employed a 100-fs Ti:sapphire laser system with a central wavelength of 783 nm, a repetition rate of 1 kHz, and a maximum pulse energy of 0.5 mJ. This pulse was down-chirped to 130 fs. The linearly polarized pump beam was collimated with a waist size of 1.38 mm and entered into a Pyrex-glass cell, measuring 60 mm in length, containing Rb vapor. The temperature of the cell was set to 180 °C. The blue light at the exit of the cell was imaged at a magnification of 1.5× onto the screen of a complementary metal-oxide semiconductor (CMOS) camera (Thorlabs DCC1645C or DCC3240M) by a standard 4f-lens configuration without any significant distortion of its wave front. To produce the blue-light interferogram, a Michelson interferometer, displayed in Fig. 1(e), was inserted between the 300-mm focal lens and the CMOS camera. Micrometers were attached in one arm of the interferometer so that the relative displacement between the two beams from both arms could be precisely adjusted.

For the blue-light emission, the values of θ_{FWM} and θ_{G} are calculated to be 0.6 and 17 mrad, respectively, satisfying the condition $\theta_{\mathrm{FWM}} \ll \theta_{\mathrm{G}}$ in Fig. 1(b). In the blue-light transverse beam profile, we define the coherent region, R_c, and its radius is calculated to be $\omega_{\mathrm{c}} = 1.5\lambda/\pi\theta_{\mathrm{FWM}} \approx 300$ μm. Note that the magnification factor of 1.5× is included.

We first recorded the spatial profiles of the blue-light intensity at a distance of 180 mm from the end face of the cell. As shown in Figs. 2(b)–2(d), the blue-light intensity profiles changed with an increase of the pump-pulse power in a similar manner to that in Ref. [16]. To analyze it, we employed the same approach adopted in Ref. [18]. Briefly, we calculated the time evolution of the atomic density operator $\hat{\rho}$ and the Rabi frequency Ω by numerically solving the coupled Maxwell-Bloch equations:

$$\frac{\partial \hat{\rho}}{\partial t} = -\frac{i}{\hbar}[\hat{V}(t), \hat{\rho}] - \sum_i \sum_j \Gamma_{ij}(1-\delta_{ij})\rho_{ij}|i\rangle\langle j|, \quad (1)$$

$$\frac{\partial \Omega_{ij}}{\partial z} = i\eta_{ij}\rho_{ij}, \quad (2)$$

with the Hamiltonian given by

$$\frac{\hat{V}(t)}{\hbar} = \sum_{J=1/2,3/2} \sum_{J'=3/2,5/2} -\Omega_{6P_J5S}|6P_J\rangle\langle 5S| - \Omega_{6P_J5D_{J'}}|6P_J\rangle\langle 5D_{J'}| + \mathrm{c.c.} \quad (3)$$

Γ and η in Eqs. (1) and (2) are the dephasing rate and the coupling constant between the atomic polarization and the Rabi frequency, respectively. The initial state of $\hat{\rho}$ is assumed to be the coherent superposition of 5S, 5P, and 5D states created by the the pump-pulse irradiation. It should be noted that the populations of 5P states do not directly affect the subsequent decay process. Further, we applied the mean-field approximation. More specifically, we introduced the constant Rabi frequency of $\Omega_{6P_J5D_{J'}}$ at $z = 0$ and ignored the amplitude and phase fluctuations of the infrared light. The blue-light intensity, $\int |\Omega_{6P_{3/2}5S}|^2 dt$, is plotted on the left axis in Fig. 2(a) as a function of the peak intensity of the pump pulse. The blue-light intensity showed an oscillatory behavior due to the Rabi oscillations during the 5S-5D two-photon absorption, which was reported in Ref. [16]. From the measured pump-beam size

and the power, the spatial profiles of the blue-light intensity were reproduced in Figs. 2(e)–2(g). For all cases, the peak intensities were multiplied by a factor of 0.81 to match the experimental results.

We next calculated the relative phase of the blue-light electric field, which is represented on the right axis of Fig. 2(a). One can observe the monotonical phase change with respect to the pump-pulse intensity. As will be clarified in the following discussion, this phase shift is a direct consequence of the phase shift of the $5D$ state with respect to the $5S$ state during the pump-pulse excitation. When $\rho_{5D5S}(z,t)$ is multiplied by an arbitrary phase factor, $\exp(-i\phi)$, with $\Omega_{5D6P}(z,t)$ left unchanged in Eqs. (1) and (2), $\Omega_{6P5S}(z,t)$ is then multiplied by $\exp(-i\phi)$, indicating that the $\rho_{5D5S}(z,t)$ phase is transferred to $\Omega_{6P5S}(z,t)$. It should be emphasized that the $\Omega_{5D6P}(z,t)$ phase actually varies shot by shot in a random manner because $\Omega_{5D6P}(z,t)$ represents a SF field. This will be discussed later based on the single-shot experiments.

To prove this phase transfer, we conducted experiments to measure the blue-light wave front from its interferogram. The experimental and simulated results are summarized in Figs. 3(a)–3(f) and Figs. 3(g)–3(l), respectively. Figure 3(a) shows the spatial profile of the blue-light intensity recorded by blocking one side of the two optical paths in the Michelson interferometer. Figures 3(b)–3(f) display interferometric fringes generated by the two beams from both paths, of which the light-propagating axes were tilted with each other by 2 mrad in the YZ plane in Fig. 1(e). The two beams were then spatially overlapped at the same position on the detector plane [Fig. 3(d)], while one beam was shifted with respect to the other beam by 150 μm to the left [Fig. 3(b)], to the right [Fig. 3(c)], upward [Fig. 3(e)], and downward [Fig. 3(f)]. In the simulated results, a tilting angle of 1.2 mrad and a spatial shift of 270 μm were assumed. In Fig. 3(d), the fringes are straight and parallel with equally spaced intervals. On the other hand, in Figs. 3(b) and 3(c), the fringes are distorted asymmetrically with respect to the central vertical axis, which are in agreement with the simulated results in Figs. 3(h) and 3(i), respectively. In contrast, Figs. 3(e) and 3(f) show fringes that are distorted symmetrically with respect to the central vertical axis. In order to compare the experimental and simulated results in more detail, we selected one fringe, indicated by a white arrow, from each of the interferograms given in Figs. 3(b), 3(c), 3(e), 3(f), 3(h), 3(i), 3(k), and 3(l). For all of the selected fringes, we derived the vertical peak position at each horizontal position. The results are summarized in Figs. 3(m) and 3(n) for the experimental and the simulated results, respectively. The vertical axes of Figs. 3(m) and 3(n) are normalized by the fringe intervals given in Figs. 3(d) and 3(j), respectively. The simulated results well reproduced the experimental results, except that the amount of phase shifts was larger in the experimental results than in the simulated results. This discrepancy might be ascribed to the slightly elliptical shape of the pump beam or the blue-light beam divergence. We performed similar experiments when the cell temperature was decreased from 180 °C to 140 °C. Although the blue-light intensity reduced to less than 1/10, the fringes were distorted in a similar manner. Thus, we eliminated the possibility where the observed distortions originate in the nonlinear propagation effects in the cell.

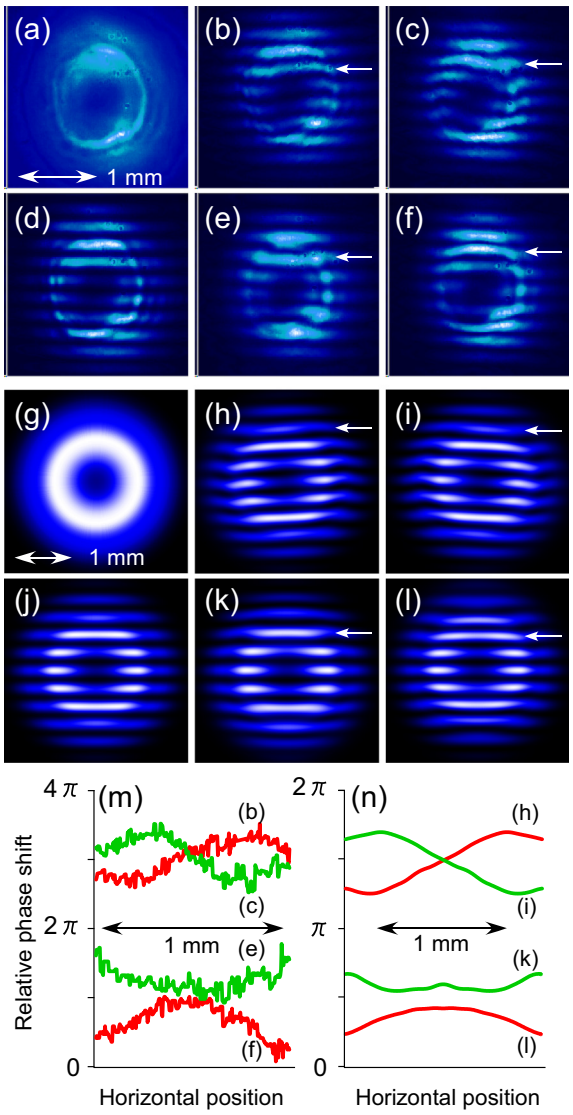

FIG. 3. (a) Experimental result of the blue-light intensity profile. (b)–(f) Blue-light interferograms recorded at a different spatial displacement between the two beams from both optical paths of the interferometer [see Fig. 1(e)]. The beams are recorded at the same position (d), and then shifted by about 150 μm to the left (b), to the right (c), upward (e), and downward (f). The pump-pulse power is fixed at 86 mW. (g) The simulated result to reproduce (a) with a peak intensity of 30 GW/cm^2 in Fig. 2(a). (h)–(l) The simulated interferograms to reproduce (b)–(f), respectively. (m) Relative phase shifts of the selected fringes indicated by a white arrow in (b), (c), (e), and (f), plotted as a function of the horizontal position. (n) Same as (m) but the fringes are selected from (h), (i), (k), and (l).

We conducted another set of experiments, where the pump-pulse power was changed while the spatial shift was fixed at the same condition as in Fig. 3(b). The results are shown in Figs. 4(a)–4(c), together with the corresponding simulated results given in Figs. 4(d)–4(f). The fringes were almost straight at the low pump-pulse power, as is the case in Fig. 4(a). By increasing the pump-pulse power, the intensity profile became ring shaped and the fringes began to appear distorted. This behavior was reproduced in the simulation. These results

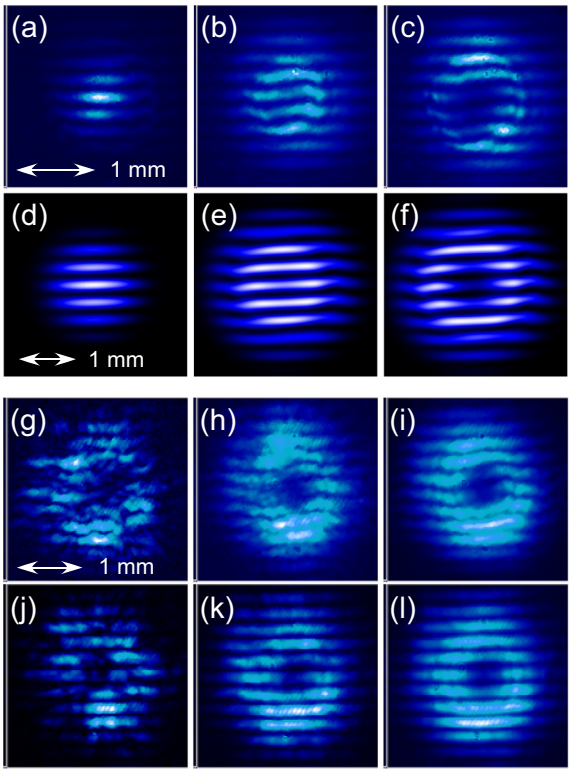

FIG. 4. (a)–(c) Blue-light interferograms recorded at different pump-pulse powers of 24 mW (a), 73 mW (b), and 86 mW (c). The spatial displacement is fixed at the same position as that in Fig. 3(b). (d)–(f) Simulated interferograms to reproduce (a)–(c), with the peak intensity of 8.5 GW/cm^2 (d), 26 GW/cm^2 (e), and 30 GW/cm^2 (f) in Fig. 2(a), respectively. (g)–(l) Single-shot [(g) and (j)], 10-shot averaged [(h) and (k)], and 100-shot averaged [(i) and (l)] blue-light interferograms recorded at pump-pulse powers of 86 mW. For (g)–(i) and (j)–(l), the spatial shift is fixed at the same position as that in Figs. 3(b) and 3(d), respectively.

exclude any possibility that the blue-light wave fronts were distorted by the focusing or defocusing effect of the blue light itself. The agreement between experimental and simulated results supports our model, where the phase of the 5*S*-5*D* wave packets is imprinted on the blue-light phase.

To provide a detailed insight about the blue-light emission beyond the scope of the mean-field physics discussed above, we conducted single-shot experiments. The results are summarized in Figs. 4(g)–4(l). In Figs. 4(g)–4(i), two beams were relatively shifted similar to that in Fig. 3(b), whereas in Figs. 4(j)–4(l), they were overlapped similar to that in Fig. 3(d). Figures 4(g), 4(h), and 4(i) correspond to single-shot, 10-shot averaged, and 100-shot averaged images, respectively. The same is true for Figs. 4(j), 4(k), and 4(l). In the single-shot images, the fringes in Fig. 4(g) are less clear when compared to those in Fig. 4(j). This can be explained by considering the aforementioned coherent region R_c. We assume that the blue-light transverse beam profile contains several R_c's and that these positions fluctuate in a shot-to-shot manner. Furthermore, the local blue-light electric fields in one R_c have no phase relation to those of another R_c. Under these assumptions, the single-shot images are classified into three cases. When the spatial shift Δl between the two beams is considerably smaller than the diameter of R_c, $\Delta l \ll 2\omega_c$, any of the local electric fields in any R_c of one beam overlap those in the same R_c of the other beam, producing fringes that are robust to shot-to-shot fluctuation. This is the case presented in Fig. 4(j). In contrast, when $\Delta l > 2\omega_c$, the local electric fields in different R_c's of the two beams always overlap. The fringes fluctuate shot-to-shot, contributing to the background signal on average. When $0 < \Delta l < 2\omega_c$, the robust fringes gradually become clear compared to the background signal during the averaging procedure. This is the case presented in Fig. 4(i). In our configuration, $\omega_c \approx 300\ \mu$m, which is consistent with the above analysis.

Now we can answer the two questions raised in the introduction. For the first question, the blue-light fields are locally coherent in the transverse beam profile, and the coherent region R_c differs randomly in every shot. For the second question, the phase of the 5*S*-5*D* wave packets created during the excitation process is transferred to the blue-light phase in each R_c. In particular, the intensity-dependent phase shift originating in a nonlinear atomic response causes the spatially dependent phase shift of the wave packets, which distorts the blue-light local wave fronts, in the case of strong excitations. Furthermore, the fringe patterns approach those predicted by the mean-field theory during the averaging procedure because this local connection of the blue-light phase to the phase of the wave packets is robust against shot-to-shot fluctuations. The above results indirectly demonstrate that the phase of the infrared light (upper SF field) is uniform in each R_c.

In conclusion, we measured the wave fronts of the blue light resulting from YSF in Rb atoms. The observed fringes were reproduced by the simulation based on the mean-field theory, demonstrating the phase transfer from the initially prepared wave packets to the blue-light fields. The single-shot experiments clarified the dimension of the R_c, which was consistent with that estimated from the FWM condition. These results pave the way for realizing a fully coherent SF field with an arbitrarily controlled spatial mode. Our method is versatile and can be applied to other SF physical systems to unveil the phase properties of SF fields and to investigate the SF dynamic by eliminating the complicated transverse effects.

This work was financially supported by JSPS KAKENHI Grant No. 18K04984 and JKA and its promotion funds from KEIRIN RACE.

[1] R. H. Dicke, Phys. Rev. **93**, 99 (1954).
[2] R. G. DeVoe and R. G. Brewer, Phys. Rev. Lett. **76**, 2049 (1996).
[3] J. Eschner, Ch. Raab, F. Schumidt-Kaler, and R. Blatt, Nature (London) **413**, 495 (2001).
[4] J. A. Mlynek, A. A. Abdumalikov, C. Eichler, and A. Wallraff, Nat. Commun. **5**, 5186 (2014).
[5] C. Bradac, M. Johnsson, M. van Breugel, B. Baragiola, R. Martin, M. L. Juan, G. Brennen, and T. Volz, Nat. Commun. **8**, 1205 (2017).

[6] A. Angerer *et al.*, Nat. Phys. **14**, 1168 (2018).
[7] J. Kim, D. Yang, S. Oh, and K. An, Science **359**, 662 (2018).
[8] J. G. Bohnet, Z. Chen, J. M. Weiner, D. Meiser, M. J. Holland, and J. K. Thompson, Nature (London) **484**, 78 (2012).
[9] M. Gross and S. Haroche, Phys. Rep. **93**, 301 (1982).
[10] F. P. Mattar, H. M. Gibbs, S. L. McCall, and M. S. Feld, Phys. Rev. Lett. **46**, 1123 (1981).
[11] J. H. Brownell, X. Lu, and S. R. Hartmann, Phys. Rev. Lett. **75**, 3265 (1995).
[12] A. I. Lvovsky, S. R. Hartmann, and F. Moshary, Phys. Rev. Lett. **82**, 4420 (1999); A. I. Lvovsky, Ph.D. thesis, Columbia University, 1998.
[13] J. R. Harries *et al.*, Phys. Rev. Lett. **121**, 263201 (2018); B. Gai, S. Hu, J. Liu, R. Cao, J. Guo, Y. Jin, and F. Sang, Opt. Commun. **374**, 142 (2016); Z. Yi, P. K. Jha, L. Yuan, D. V. Voronine, G. O. Ariunbold, A. M. Sinyukov, Z. Di, V. A. Sautenkov, Y. V. Rostovtsev, and A. V. Sokolov, *ibid.* **351**, 45 (2015); G. O. Ariunbold, V. A. Sautenkov, and M. O. Scully, Opt. Lett. **37**, 2400 (2012); G. O. Ariunbold, M. M. Kash, V. A. Sautenkov, H. Li, Y. V. Rostovtsev, G. R. Welch, and M. O. Scully, J. Opt. Soc. Am. B **28**, 515 (2011); C. V. Sulham, G. A. Pitz, and G. P. Perram, Appl. Phys. B **101**, 57 (2010); D. Felinto, L. H. Acioli, and S. S. Vianna, Opt. Lett. **25**, 917 (2000).
[14] G. O. Ariunbold, M. M. Kash, V. A. Sautenkov, H. Li, Y. V. Rostovtsev, G. R. Welch, and M. O. Scully, Phys. Rev. A **82**, 043421 (2010); L. Yuan, B. H. Hokr, A. J. Traverso, D. V. Voronine, Y. Rostovtsev, A. V. Sokolov, and M. O. Scully, *ibid.* **87**, 023826 (2013).
[15] M. O. Scully, E. S. Fry, C. H. Raymond Ooi, and K. Wódkiewicz, Phys. Rev. Lett. **96**, 010501 (2006); M. O. Scully and A. A. Svidzinsky, Science **325**, 1510 (2009).
[16] K. Kitano and H. Maeda, Opt. Express **25**, 23826 (2017).
[17] M. S. Feld and J. C. MacGillivray, *Coherent Nonlinear Optics, Superradiance* (Springer-Verlag. Berlin/Heidelberg/New York, 1980).
[18] K. Kitano and H. Maeda, Phys. Rev. A **97**, 063418 (2018).